Research Square

Preprints are preliminary reports that have not undergone peer review.
They should not be considered conclusive, used to inform clinical practice,
or referenced by the media as validated information.

# A Strategy for Synergistic Photothermal-Photocatalytic: Contactless Photocatalytic Reactor for CO 2 Reduction with Seawater or Wastewater into HCOOH

**Kun Liu**

L_iukun@163.com

China Huaneng Group Co., Ltd. (China)

**Anjie Shu**

China Huaneng Group Co., Ltd. (China)

**Liang Zhao**

China Huaneng Group Co., Ltd. (China)

**Bo Qiu**

China Huaneng Group Co., Ltd. (China)

**Jiefeng Wang**

China Huaneng Group Co., Ltd. (China)

**Research Article**

**Keywords:** photocatalytic reactor, contactless, CO2 reduction, heat radiation

**Posted Date:** August 13th, 2026

**DOI:** https://doi.org/10.21203/rs.3.rs-10340093/v1

**License:** This work is licensed under a Creative Commons Attribution 4.0 International License.
Read Full License

**Additional Declarations:** No competing interests reported.

# A Strategy for Synergistic Photothermal-Photocatalytic: Contactless Photocatalytic Reactor for $CO_2$ Reduction with Seawater or Wastewater into HCOOH

Kun Liu[1,*] Anjie Shu[1,*], Liang Zhao[1], Bo Qiu[1], Jiefeng Wang[1]

[1]China Huaneng Group Energy Research Institute, Xiong'an, Hebei, China

## Abstract

Photocatalytic reduction of $CO_2$ with $H_2O$ into value-added chemicals represents one of the most promising routes for solar energy utilization. However, the intrinsic disparity in mass transfer rates between gaseous $CO_2$ and liquid water on catalyst surfaces, combined with the presence of impurities in water that readily trigger competing side reactions, typically results in sluggish reduction kinetics and hinders practical application. Herein, a synergistic photothermal-photocatalytic strategy is developed by designing a contactless photocatalytic reactor that concurrently synchronizes and enhances mass transfer while expanding the scope of usable water sources. Specifically, heat radiation-induced evaporation is exploited to accelerate the transport of both reactants and products, thereby relaxing the purity requirements for the water feedstock and sustaining efficient $CO_2$ reduction rates even with seawater and wastewater. Importantly, the diffusion rates of vaporized $H_2O$ and $CO_2$ reach the same

*Corresponding author.

E-mail addresses: kun_liu@chng.com.cn

order of magnitude, effectively eliminating the mass-transfer mismatch. Under full-spectrum irradiation in a reactor with a 1 $cm^2$ irradiation area, the $CO_2$-to-formic acid production rates using pure water, simulated seawater, and simulated wastewater reach 680.7, 645.3, and 663.0 $\mu mol\ g^{-1}\ h^{-1}$, respectively. This work not only demonstrates the valorization of wastewater resources but also opens a new avenue for integrated photocatalysis and photothermal conversion.

Keywords: photocatalytic reactor, contactless, $CO_2$ reduction, heat radiation

# Introduction

Photocatalysis represents one of the most important routes for converting solar energy into chemical energy[1,2]. The efficiency of photocatalytic processes is fundamentally governed by light absorption-dictated by the bandgap—and charge carrier dynamics, which are strongly influenced by surface properties[3-6]. Consequently, extensive efforts have been devoted to catalyst structural engineering, including heterojunction construction, porous surface architecture, and elemental doping[7-10]. However, wide-bandgap semiconductors that often offer favorable selectivity are inherently restricted to ultraviolet absorption[11], meaning that more than 50% of solar energy is dissipated as heat through photothermal conversion[12,13]. This has motivated considerable interest in reactors that couple photothermal and photocatalytic effects within a single device, particularly exploiting heat to accelerate electron migration and reactant transport[14-16]. Beyond these factors, mass transfer of reactants remains a critical rate-limiting step in photocatalysis. Although capillary-force-driven transport can enhance mass transfer, it still falls notably short of the performance achieved under forced convection[17]. More importantly, current photocatalytic reactor designs are largely tailored to specific reactions—photocatalytic water splitting for hydrogen production being a prominent example[18], which limits their adaptability to other processes. The development of universal photocatalytic reactors therefore constitutes a critical challenge.

Currently, slurry-type photocatalytic reactors are the most widely adopted configuration[19,20]. However, light penetration through the bulk solution leads to photon

losses from refraction and reflection, and a portion of the absorbed photons is subsequently dissipated as heat (Fig.1a)[17,21]. Floating photocatalytic reactors[22], which can focus light in a two-dimensional plane, avoid photon escape and reduce the large heat loss caused by excessive solution contact with the catalyst (Fig.1b)[17]. Nevertheless, their practical deployment is limited by the need for forced convection, photocatalyst leaching, and still substantial heat loss[23]. These heat losses primarily originate from the temperature gradient between the catalyst and its surrounding medium, conductive heat transfer from the 2D plane to excess reactants, and radiative exchange with the environment. Against this backdrop, photocatalytic $CO_2$ reduction with $H_2O$ is an attractive strategy to mitigate the greenhouse effect while producing valuable chemicals[24-26], especially given the abundance and low cost of water[27]. More importantly, the $CO_2$–$H_2O$ reaction is a gas–liquid system at room temperature and representative of many chemosynthetic processes[28,29]. Therefore, developing a photocatalytic reactor with high mass transfer rates and low heat loss, using $CO_2$ reduction as a model validation, is a logical and effective pathway.

Herein, a synergistic photothermal–photocatalytic strategy was employed to design and construct a contactless photocatalytic reactor (Fig. 1c). Specifically, the catalyst was directly loaded onto a 2D plane to minimize photon escape. Thermal radiation from the photothermal effect was utilized to vaporize the liquid reactants, with the resulting vapor subsequently transferred to the active sites by diffusion. This contactless configuration reduces the temperature difference between the gas-phase reactants and the catalyst, enabling reactant pre-activation, and simultaneously cuts off

conductive heat loss to the excess low-temperature liquid. Furthermore, the transport paths and distances of the reactants can be controlled to achieve a balanced feed ratio. Using $CO_2$ and $H_2O$ reduction to formic acid as a probe reaction, the production rate reached 680.7 μmol $g^{-1}$ $h^{-1}$, far surpassing that of a conventional slurry reactor (42.4 μmol $g^{-1}$ $h^{-1}$). Remarkably, when simulated seawater and wastewater were used as the reactant sources, the formic acid production rates still reached 645.3 μmol $g^{-1}$ $h^{-1}$ and 663.0 μmol $g^{-1}$ $h^{-1}$, respectively. These results confirm that the contactless photocatalytic reactor delivers superior performance, benefiting from enhanced mass transfer, efficient light absorption, and reduced photon and heat losses. Moreover, by leveraging the evaporation-driven transport mode, this reactor circumvents the need for water purification and can directly utilize seawater or even wastewater when coupled with water oxidation. Thus, this contactless photocatalytic reactor opens a new avenue for gas–liquid reactions, eliminating the stringent requirements for water quality and complex purification steps.

## Results and Discussion

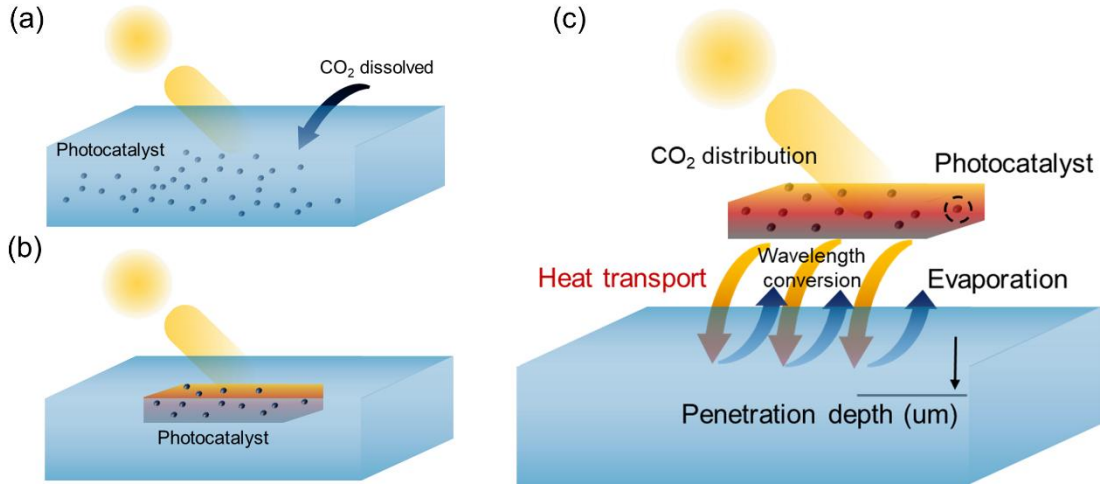



Fig.1 Schematic diagrams of different photocatalytic reactors, (a) slurry photocatalytic

reactor, (b) floating photocatalytic reactor, and (c) contactless photocatalytic reactor.

The contactless photocatalytic reactor (CPR) forms a two-dimensional catalytic plane (TCP) by loading a catalyst ($TiO_2$/MXene) into a two-dimensional porous medium that is directly exposed to solar irradiation to facilitate direct activation of the catalyst. The wavelengths beyond the bandgap are directly converted into heat by photothermal conversion and then diffused to the surroundings by heat conduction. The TCP prevents heat loss due to its own heat resistance, so the heat is confined to the catalyst surface. Even if the heat spreads to the lower interface of the TCP, the separation from the liquid reactants prevents continuous heat consumption. Instead, heat radiation transfers heat to the solution via electromagnetic waves, which induces the vaporization of the lower solution, replacing the water purification step. In addition, according to the Beer-Lambert law, the penetration depth of electromagnetic waves into the solution depends on the wavelength, and the penetration depth of radiation wavelengths into water is limited to the micrometer level, while the penetration depth of sunlight wavelengths reaches the meter level. More importantly, the SPR requires $CO_2$ to be dissolved, and solubility is negatively correlated with temperature, i.e., photothermal action triggers a decrease in $CO_2$ concentration. In contrast, CPR is unaffected because $CO_2$ no longer needs to be dissolved in water, and the ratio of reactants $CO_2$ to $H_2O$ is no longer limited by solubility. It is well known that the feed ratio affects the mass transfer resistance and the reduction rate, and when the ratio of $CO_2$ to $H_2O$ is close to 1:1, it increases the reaction rate while adjusting the optimal concentration and decreases the mass transfer resistance. Accordingly, CPR can be

realized by adjusting the distance of heat radiation transfer. The heat radiation transfer not only isolates the heat consumption of the liquid phase reactants, but also increases the mass transfer rate and internal energy of the reactants, since the mass transfer rate of the gas phase reactants is much higher than that of the liquid phase reactants, which also eliminates the need for additional energy input steps such as stirring.

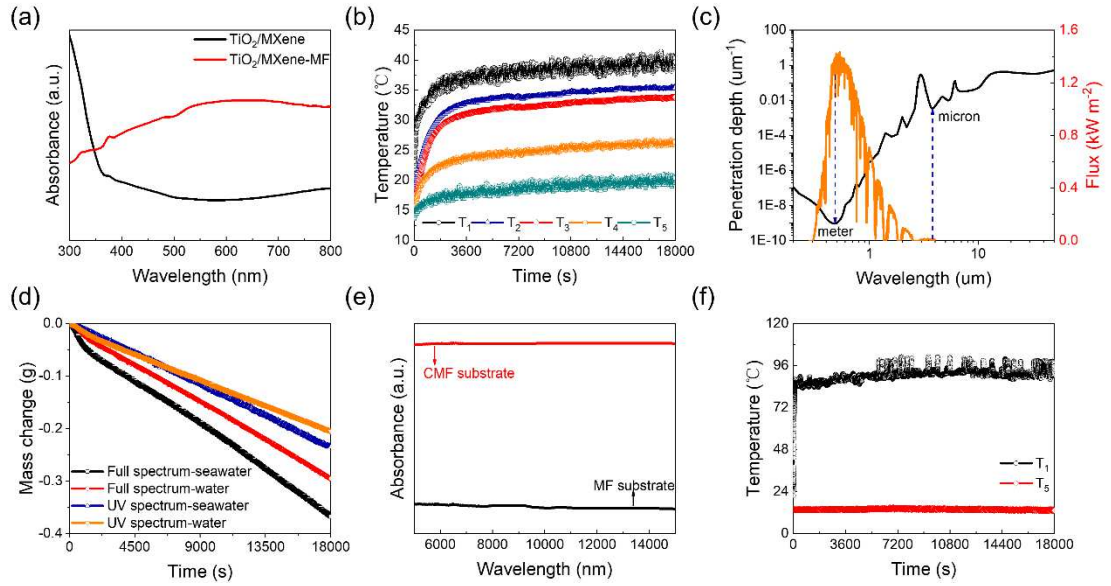



Fig.2 (a) Light absorbance of $TiO_2$/MXene and $TiO_2$/MXene-MF. (b) Temperature response of different interfaces of $TiO_2$/MXene-MF. (c) Penetration depth of the solar spectrum. (d) $TiO_2$/MXene-MF-induced mass change. (e) Comparison of the optical absorbance of $TiO_2$/MXene after loading on MF or CMF substrates. (f) Temperature response of $TiO_2$/MXene-CMF.

The expansion of light absorption makes the temperature of CPR higher than that of SPR, and also improves the efficiency of solar energy utilization. Most importantly, the $TiO_2$/Mxene loading on MF does not change the light absorption characteristics. As shown in Fig.2a, the $TiO_2$/Mxene powder has better light absorption performance before 400 nm due to the limitation of catalyst band gap. And after loading on MF

($TiO_2$/Mxene MF), the TCP reduces the optical loss and exhibits broader full-spectrum absorption characteristics. In particular, the absorption in the visible region (300-800 nm) shows stability, which compensates for the lack of absorbable photons in the carbon substrate (MXene). At the same time, the two-dimensional interface is more favorable for photothermal conversion, reducing heat loss and improving the stability of photothermal conversion. For this purpose, the temperature trends at different locations of the CPR were tested, where the temperature at the top surface of $TiO_2$/MXene-MF was $T_1$, the temperature at the bottom interface was $T_2$, the temperature at the solution surface was $T_3$, the temperature at the bottom surface of the solution was $T_4$, and the ambient temperature was $T_5$ (Fig.2b). Under full-spectrum irradiation, the photothermal temperature showed a steady increase, and the interfaces in the heat transfer path also realized a steady temperature enhancement. And the photothermal temperature of the surface increased rapidly and gradually leveled off in a short time, and the rate of temperature increase was much higher than that of the SPR (Fig.S1). Under the irradiation of UV light, the temperature of photothermal conversion is lower (Fig.S2). Meanwhile, the temperature difference between the different surfaces provide the impetus for the reactant transport. Specifically, the temperature difference ($T_1$-$T_2$) between the upper and lower interfaces of $TiO_2$/MXene-MF minimizes the heat loss due to heat conduction. The temperature difference between the lower interface and the solution ($T_2$-$T_3$) also applies heat radiation to trigger the vaporization of the reactants, forcing the reactants to diffuse through the upper interface, which increases the mass transfer rate and also reduces the energy consumption required for enhanced

mass transfer. Furthermore, according to Kirchhoff's law, the emissivity at the lower interface is equal to the light absorption rate, i.e., a low absorption rate represents a low radiation loss. The temperature difference between the bottom interface and the reactants provides a temperature difference driving force for increasing the internal energy of the reactants, which realizes the pre-activation of the reactants. According to Beer-Lambert law, the penetration depth of solar radiation spectrum can reach 40 m, while the penetration depth of infrared radiation wavelength is less than 300 um. Therefore, CPR can maximize the conversion of low-content heat radiation loss into heat, which is confined to the top of the solution. The temperature difference between the top and bottom of the solution is further evidence of the photon penetration properties ($T_3$-$T_4$). In addition, even in the UV spectrum, there are many photons that cannot be absorbed and converted to heat e.g., (Fig.S3). Although the temperature under UV radiation is lower and the temperature difference is significantly reduced, the temperature difference between interfaces remains due to spatial isolation.

The reactant supply rate was then tested, i.e., the reactant vaporization mass was tested under different light. As shown in the Fig.2d, the water transport rate reached 0.016 mg/s under the full spectrum, which ensured sufficient reactant supply. The fact that there is still sufficient reactant supply (0.011 mg/s) even when relying on UV light alone shows that UV light also induces photothermal effects and at the same time proves that using the full spectrum improves the reactant supply rate. This also provides better selectivity for feed ratio adjustment and expands the spectrum for photothermal conversion. In addition, the exchange of heat radiation between two planes is positively

correlated with the viewing angle factor according to Planck's law [30]. And the viewing angle factor is determined by the distance between the planes, which means that changing the gap between the lower interface of $TiO_2$/MXene-MF and the water surface can adjust the transport rate of reactants. In addition, the gap between the lower interface and the water surface eliminates the influence of the water source on the catalyst and also reduces the requirement of an aqueous solution, i.e., the purification of pure water can be achieved by taking advantage of the non-vaporability of the solute. For example, seawater solution is one of the best options. For this purpose, the rate of reactant supply when seawater is used as the reactant was verified for both full and UV spectra. As shown in Fig.2d, the product supply rate reached 0.021 mg/s for the full spectrum and 0.011 mg/s for the UV spectrum, which proves that seawater can be a direct substitute for pure water in CPR and the supply rate is also higher than that of pure water. This is due to the dissolution of NaCl salts, which changes the absorption properties of light. Therefore, when seawater is used as a reactant, the supply rate is increased while the intermediate step of desalination is eliminated.

Secondly, the CPR can also achieve a higher temperature response by carbonizing the surface to increase the light absorption of the surface. However, the reactant feed rate increases accordingly, which tends to cause an imbalance in the feed ratio. As shown in Fig.2e, $TiO_2$-MXene loaded on CMF substrate forms $TiO_2$-MXene/CMF, which not only extends the light absorption range but also increases the light absorption rate, especially compensating for the loss of visible spectrum. Especially in the spectral range of 200-800 nm, a full spectrum of absorption is revealed. The temperature after

photothermal conversion is greatly improved, and $T_1$ can reach 91.5°C (Fig.2f). Similarly, the temperature after photothermal conversion can reach 42°C even under the irradiation of UV spectrum (Fig.S4). This also proves that most of the photons are still directly converted into heat instead of being absorbed by the catalyst for catalysis. According to Kirchhoff's law, the higher light absorption, the higher blackbody emissivity, and the high mid-infrared absorption of $TiO_2$-MXene-CMF determines its high radiant energy. The high radiant flux improves the exchange of heat radiation with the lower interface, which leads to a great increase in the reactant feed rate, and reaches 0.0157 mg/s under the condition of spectrally irradiated pure water. In addition, the reactant feed rate reaches 0.0248 mg/s when seawater is used. Even under UV light, the feed rate of seawater and water as reactants reaches 0.01 mg/s and 0.005 mg/s (Fig.S5). It is proved that CPR can realize different reactant feed rates by regulating the photothermal action, which greatly expands the application range of solar energy and opens a new channel for the photothermal action of photocatalysis. Compared with the low mass transfer rate of the SPR with excess reactants, CPR achieves an increase in the mass transfer rate and a significant increase in the reaction temperature, which is more conducive to accelerated electron migration, especially a significant increase in the heating rate. When the spectral absorbance is increased, $TiO_2$-MXene/CMF achieves a heating rate of 0.46 K/s, which minimizes the heating time of the reaction system. More importantly, the CPR will utilize the combined photothermal effect and the rapid response of heat transfer to achieve the timely operation of photocatalysis.

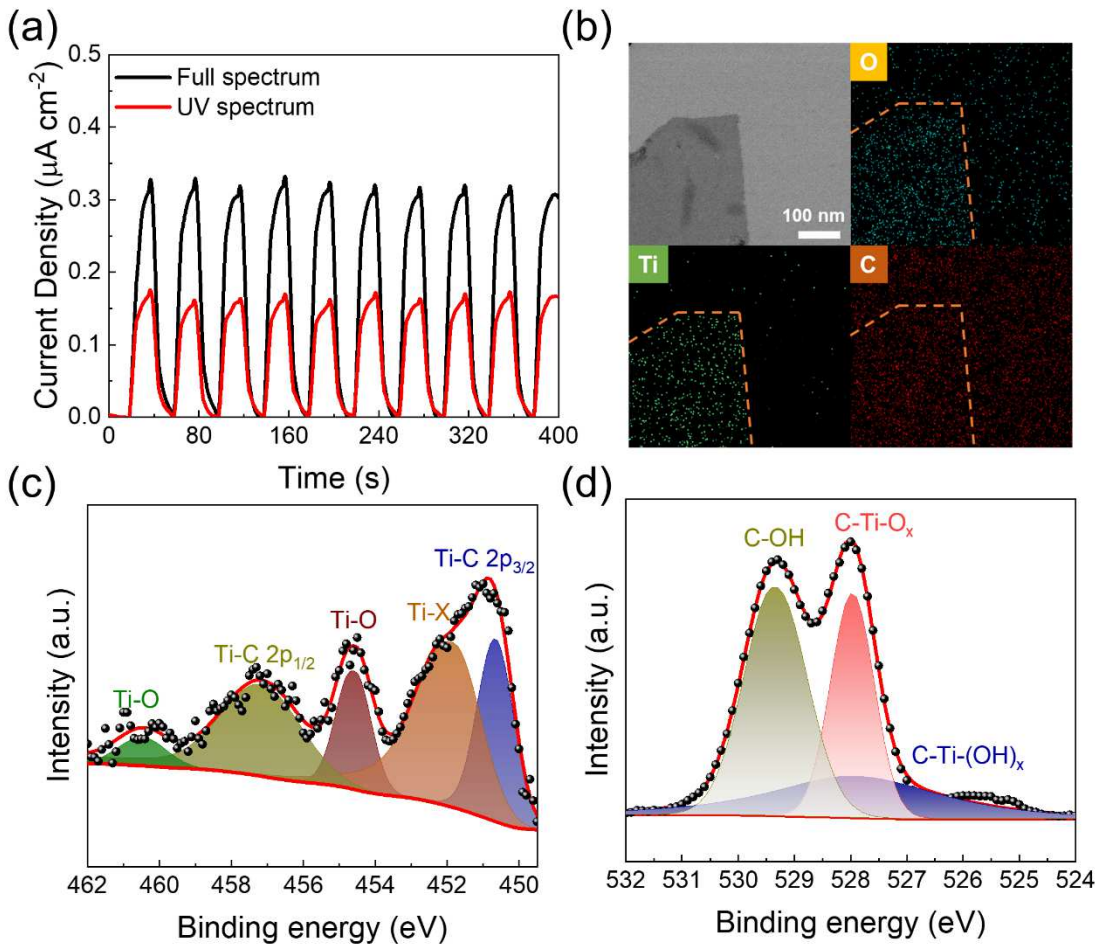



Fig.3 (a) Photocurrent test of $TiO_2$/MXene under full spectrum and UV spectrum again. (b) TEM diffraction pattern of $TiO_2$/MXene containing elements O, Ti, and C. XPS patterns of $TiO_2$/MXene with (c) Ti and (d) O elements.

The photoreduction rate of $CO_2$ is still correlated with the current density after surface electron excitation. $TiO_2$/MXene was synthesized by an in-situ oxidation strategy and applied to $CO_2$ reduction. Importantly, the choice of catalyst was determined by the reaction characteristics. For $CO_2$ reduction to formic acid ($CO_2+H_2O \rightarrow HCOOH+O_2$), the reaction characteristics limit the catalyst band gap (0.82 ev-0.61 eV).The low cost of $TiO_2$ is one of the best choices, and the synthesis strategy of MXene oxidation improves the light absorption range. Therefore, $TiO_2$/MXene was applied in $CO_2$ reduction experiments. The light absorption spectrum of $TiO_2$/MXene revealed

that the absorption boundary is located at approximately 396 nm, and based on the evaluation of Tauc plots (Fig.S6), the band gap energy of $TiO_2$/MXene was determined to be 2.1 eV. In addition, based on the Mott-Schottky test, it was elucidated that the flat band potential of $TiO_2$/MXene is -0.96 V vs. Ag/AgCl (i.e., -0.76 V vs. NHE, Fig.S7). According to the equation $E_g = E_{VB} - E_{CB}$, the valence band position was calculated to be 1.34 V vs. NHE. Based on the valence and conduction band positions, it can be concluded that $TiO_2$/MXene is thermodynamically compatible with the photoreduction of $CO_2$ for the production of formic acid.

Furthermore, the photocurrent density represents the efficiency of electron-hole photoexcitation and also determines the separation and migration behavior of electron-hole pairs, which is one of the key conditions for achieving $CO_2$ reduction. The photocurrent intensity test was carried out for $TiO_2$/MXene samples using intermittent light illumination (Fig.3a), and the photocurrent density reached 0.325 uA $cm^{-2}$ under full-spectrum light illumination. Based on electrochemical impedance spectroscopy (EIS), $TiO_2$/MXene exhibited a smaller semicircular diameter in the high-frequency region in the Nyquist plot (Fig.S8), indicating the good performance for the separation and transport of surface charge carriers. However, the absorption band edge of $TiO_2$/MXene is less than 420 nm, so most of the solar energy of the spectrum is dissipated as heat. We tested the photocurrent response profile in the UV spectrum, as shown in Fig.2a, with a photocurrent density of 0.168 uA $cm^{-2}$. Based on the light absorption properties of the semiconductor, it is shown that the light absorption threshold at 420 nm remains unchanged and the number of excited photoelectrons

remains unchanged. This indicates that the heat can reduce the photoelectron-hole complexation rate and increase the relaxation time of photoelectrons, which is more favorable for photocatalysis.

It is noteworthy that the multi-overlapping heating effect of $TiO_2$/MXene is beneficial to increase the optical current density response. Firstly, the MXene substrate of $TiO_2$/MXene is composed of material C, as evidenced by the XRD spectra (Fig.S9). The characteristic peak of MXene is located at $2\theta \approx 7°$ (002), which is consistent with what has been reported in the literature[31]. In addition, $TiO_2$ was also generated synchronously by an in-situ oxidation strategy, corresponding to a peak at 38.7° (JCPDS No. 21-1272). The Ti-O bonds grown in-situ on the C substrate contribute to the electron transfer. The TEM diffraction pattern shows that the Ti elements are uniformly distributed around the O elements (Fig. 3b). The C elements are uniformly distributed throughout the substrate, which again confirms the uniform mixing of the C substrate and the Ti elements, and the wide distribution of the C elements. Furthermore, there are obviously more C elements than O elements around Ti atoms, and Ti-O exists mainly in the form of $TiO_2$, which is consistent with the XPS results. As shown in Fig.3c, the binding energies of Ti elements are 460.5, 457.1, 454.7, 452.1, and 450.7 eV, and the corresponding characteristic peaks correspond to Ti-O, Ti-C $2p_{1/2}$, Ti-O, Ti-X, and Ti-C $2p_{3/2}$. Detailly, the peaks for Ti-C bonding are the strongest, which also proves that the cross-linking of Ti elements with C elements improves the light absorption properties while increasing the electron transport properties. Based on the XPS spectra of elemental O (Fig.3d), it was found that C-OH, C-Ti-$O_x$, and C-Ti-$(OH)_x$ correspond

to 529.3, 528, and 527.5 eV, respectively. Increasing the oxygen content improves the catalytic performance and also changes the structure of the MXene substrate. The C substrate is surrounded by F elements, as shown in Fig.S10, the C-F bond, C-O bond, and C-C bond correspond to 284.7, 282.4, and 280.9 eV, respectively. The high strength of the C-C bond proves the high C content, and also confirms that the carbon-containing substrate has the potential to improve the photothermal performance. Thus, the superimposed C-Ti element not only thermodynamically favors the reduction of $CO_2$, but also promotes the electron transfer efficiency, while the presence of C further enhances the photothermal effect.

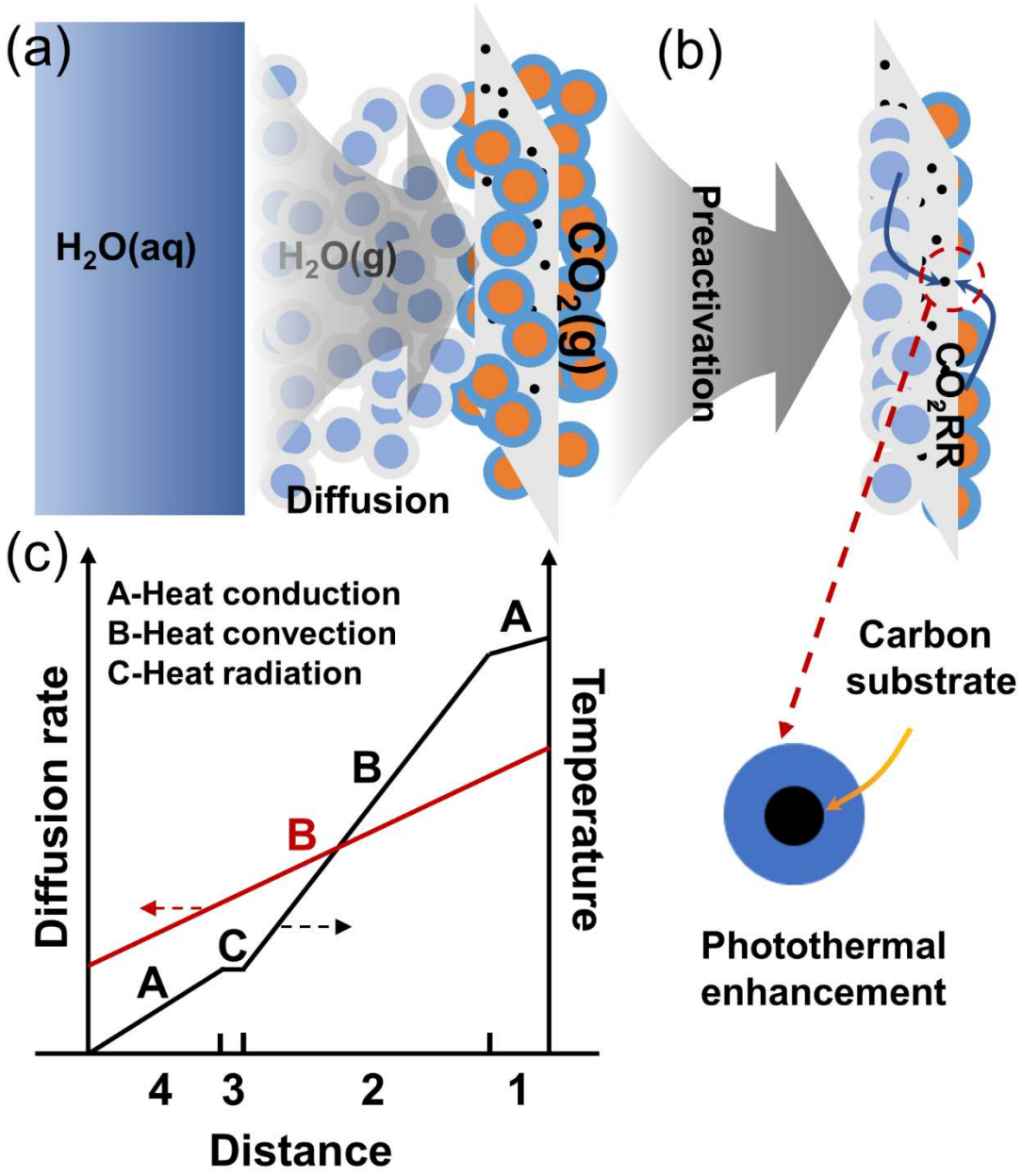



Fig.4 (a) Schematic diagram of the mechanism of action of CPR. (b) Schematic diagram of reactant pre-activation and thermal stacking in CPR. (c) Heat transfer mechanism of CPR.

The resistance to mass transfer between liquid phases replaces the resistance to mass transfer between gas phases. Although the floatable photocatalytic reactor can temporarily increase the mass transfer rate by relying on the capillary force, the capillary force is limited by the magnitude to not be able to realize long-range transport

and growth rate. Meanwhile, the adhesive force of the liquid in the tiny pores increases the difficulty of catalyst adsorption of reactants. The adsorption force between liquids is much higher than that of gases, and it is very easy to form accumulated droplets[32], which affects the feed ratio of reactants. According to Fick's law [33], the diffusion rate of the gas is much higher than that of the liquid, and CPR directly uses the free diffusion of the gas to convert it into the driving force for the mass transfer of reactants. In addition, the heat transfer process presents a temperature gradient, forcing the vaporized reactants to gradually accelerate the diffusion into the high temperature region, i.e. from the bottom layer to the surface of the catalyst. As shown in Fig.4a, the liquid water source absorbs heat and vaporization. The water molecules are transported to the active sites by free diffusion and undergo a reduction reaction with the $CO_2$ accumulated on the surface. Due to the temperature gradient in the transport path of the reactants and the continuous heat exchange of the water vapor during the heat transfer process, the internal energy and mass transfer rate of the reactants eventually increases continuously. In addition, the TCP of the CPR has intercepted photon escape, increased light absorption and enhanced photothermal conversion. The carbon substrate of the catalyst, increases the photothermal conversion, and the superimposed photothermal effect raises the temperature of the material surface, facilitating the electron migration rate (Fig.4b). The detailed heat transfer path is shown in Fig.4c, where the mode of heat exchange changes as the distance to the bottom of the liquid surface increases. There are three modes of heat conduction (A), heat convection (B) and heat radiation (C) in the full path. In detail, in path 1, the most dominant mode of heat exchange is heat

conduction, which relies on the cross-linked skeleton inside the porous medium for transmission. The heat continues to spread downward, and only water vapor after the phase change exists in path 2, and the low heat conductivity of the gas makes the heat transfer mainly rely on heat convection. The existence of temperature gradient accelerates the diffusion rate and improves the heat transfer effect of heat convection. The main heat transfer in path 3 is achieved by heat radiation from the CPR surface, and the response distance is limited to the micrometer level. After that, the heat from the upper solution is transferred downward by heat conduction (path 4), which inevitably causes a small part of heat loss. In summary, the temperature shows a decreasing gradient throughout the process, while the mass transfer rate, i.e. the diffusion rate is gradually increasing.

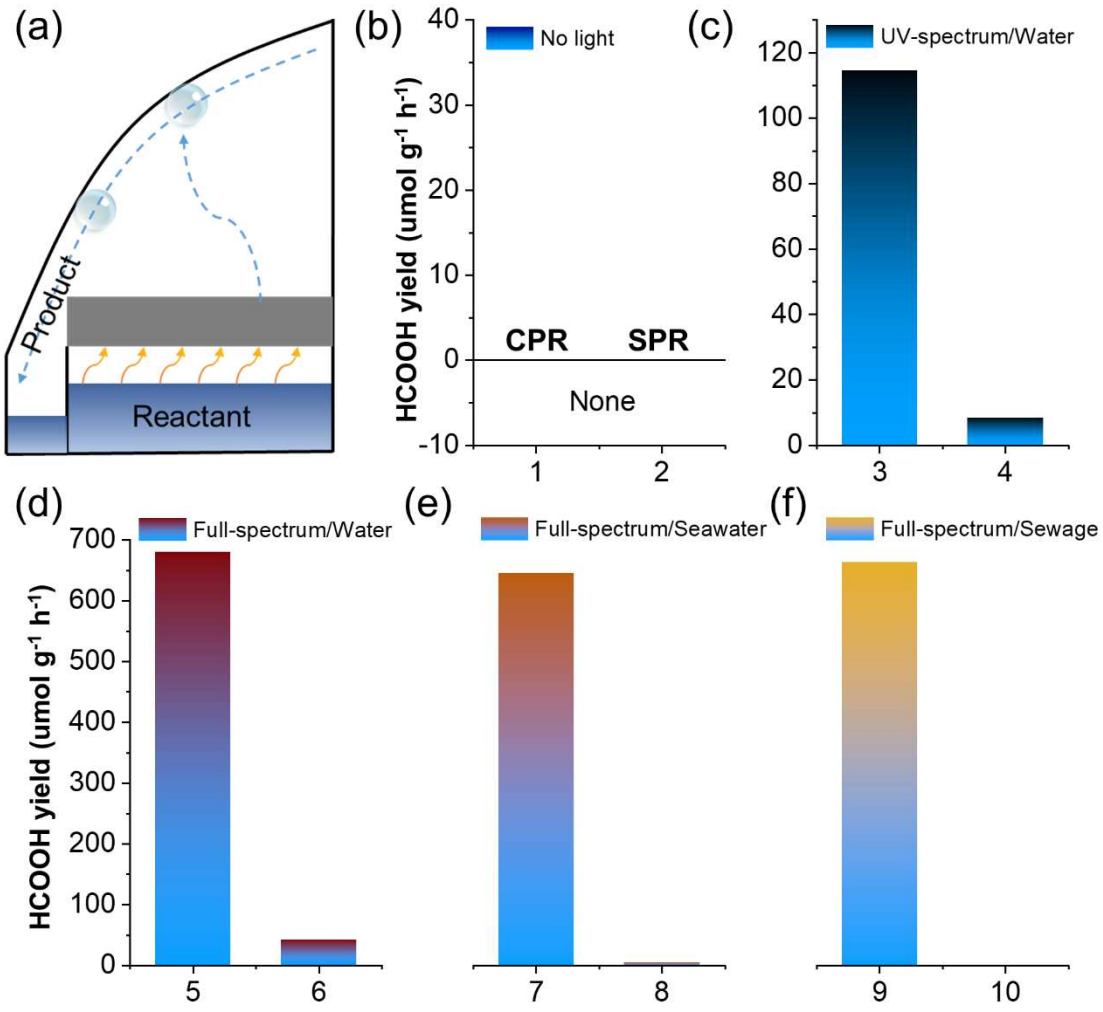



Fig.5 (a) Diagram of CPR. (b) Formic acid yield under dark conditions. (c) Formic acid yield of CPR and SPR using pure water in UV light. (d) Formic acid yield of CPR and SPR using pure water in full spectrum. (e) CPR and SPR using formic acid yield of seawater at full spectrum. (d) CPR and SPR use the formic acid yield of sewage in the full spectrum.

The multi-stage heat utilization and diffusion enhancement of CPR promoted the $CO_2$ reduction rate, and its photocatalytic properties were characterized by testing the HCOOH yield. The reactor design is shown in Fig.5a, and the reaction products were zero-condensed on the light-transmitting glass surface and refluxed to the product collection tank, where the products were tested by $^1$H NMR (Fig.S11). The formic acid

yields of CPR (Experiments 1, 3, 5, 7, 9) and SPR (Experiments 2, 4, 6, 8, 10) in different conditions were tested. First, in the no light condition, the results showed that none of the products were generated (Fig.5b), indicating that light was the only driving force to stimulate the reaction. In addition, the reduction rates under different substrates were also compared, and as shown in Fig. Fig.S12, there was no gas generation under the unloaded catalyst condition. Further, the CO2 rate after loading CMF was much higher than that of MF, proving that the enhanced photothermal conversion contributes to the photocatalytic efficiency. Therefore, the subsequent experimental tests were completed on top of the CMF substrate. Translated with DeepL.com (free version)Next, to verify the selectivity of the solar spectrum and the percentage of photothermal action, the formic acid yield under UV light was tested. Comparisons showed that with UV spectrum irradiation and application of pure water, the formic acid yield was 114.63 μ mol $g^{-1}$ $h^{-1}$ for CPR (Fig.3c) and 8.49 μmol $g^{-1}$ $h^{-1}$ for SPR. When the experiment was completed with full spectrum and pure water (Fig.5d), the formic acid yield for CPR was 680.7 μmol $g^{-1}$ $h^{-1}$, the SPR yielded 42.4 μmol $g^{-1}$ $h^{-1}$. Therefore, the photothermal effect of the full spectrum was more advantageous, especially for accelerating the electron migration, improving the mass transfer rate of reactants and products, and pre-activating the reactants. Meanwhile, the source of CPR reactants can be more extensive, and when simulated seawater was used as the reactant (Fig.5e), a high yield of about 645.3 μmol $g^{-1}$ $h^{-1}$ was still maintained, while the yield was only 4.95 μmol $g^{-1}$ $h^{-1}$ when SPR was used. When sewage water was used (Fig.5f), i.e., when multiple ions were doped, the CPR reaction rate was 663.02 μmol $g^{-1}$ $h^{-1}$ compared to 0 μmol $g^{-1}$ $h^{-}$

[1] for SPR. In addition, the light-absorbing area of CPR was only 1 $cm^2$, i.e., the highest reduction rate of $CO_2$ reached 68.07 $mol/m^2$, which can be widely applied to direct surface reduction. As a result, CPR no longer restricts the source of water, thus expanding the range of applications that combine the direct use of seawater and solar energy.

# Conclusion

In summary, a contactless photocatalytic reactor based on a synergistic photothermal-photocatalytic strategy has been developed and demonstrated to substantially outperform conventional slurry reactors for $CO_2$ reduction. By physically separating the reactant reservoir from the catalyst layer, this design eliminates the need for reactant purification and converts otherwise wasted heat radiation into a driving force that increases the internal energy of the reactants. The adjustable reactant supply accommodates different stoichiometric feed ratios, enabling adaptation to a wide range of catalytic reactions. More importantly, the multistage heat utilization of the reactor decouples catalytic performance from water purity, allowing efficient $CO_2$ reduction even when using seawater or wastewater. Accordingly, formic acid production rates of 680.7, 645.3, and 663.0 $\mu mol\ g^{-1}\ h^{-1}$ were achieved with pure water, simulated seawater, and simulated wastewater, respectively. The reactor consistently maintains its high performance across these diverse water sources, demonstrating remarkable robustness and opening a new direction for practical photocatalytic applications.

**Conflicts of interest**

There are no conflicts to declare.

**Acknowledgements**

This work was fully supported by the Huaneng Group's Science and Technology project (HNKJ24-HF38).

## Experimental Section

### Chemicals and materials.

All materials were commercially available and did not require further purification. The $Ti_3AlC_2$ powder and lithium fluoride (LiF), sodium chloride powder (NaCl), and nan sulfate powder ($Na_2SO4$) were purchased from Aladdin (China).

### Preparation of $TiO_2$/MXene.

MXene ($Ti_3C_2T_X$) is prepared by etching $Ti_3AlC_2$ with LiF and HCl. For example, 3.2 g LiF was mixed with HCl (12 mol $L^{-1}$) by stirring for 15 minutes. Subsequently, 2.00 g $Ti_3AlC_2$ was slowly added to the mixed solution. The mixture was stirred continuously at 40°C for 48 hours. The resulting acidic slurry was washed with deionized water and centrifuged at 3500 rpm for 5 minutes, and then washed with deionized water several times until the pH was ≈ 6. MXene and water were then combined in a ratio of 1:2, ultrasonically mixed, and added to a hydrothermal reactor, and heated at 180 °C for 5 hours. The final solution was filtered and freeze-dried to obtain a powder sample.

### Preparation of $TiO_2$/MXene-MF and $TiO_2$/MXene-CMF.

The melamine foam (MF) was cut into 20×20×5 $mm^3$ pieces, added to the ethanol solution, and then transferred to a tube furnace and vacuum-dried at 80°C for 300

minutes. Then, 30 mg of $TiO_2$/MXene was added to 30 mL of water and mixed well, and finally sprayed uniformly on the surface of the melamine foam to form $TiO_2$/MXene-MF. The MF was heated in a tube furnace at 500°C for 5 h with a heating rate of 5°C/min to form CMF. After that, CMF was added to ethanol solution with ultrasonic vibration and then transferred to a tube furnace for 300 min at 80°C. The CMF was heated for 5 h with a temperature increase rate of 5°C/min to form CMF. transferred to a tube furnace and dried under vacuum at 80°C for 300 min. Finally, 30 mg of $TiO_2$/MXene was added to 30 mL of water and mixed well, and finally sprayed uniformly on the surface of melamine foam to form $TiO_2$/MXene-CMF.

**Photocatalytic experiment for SPR**.

The catalyst (10 mg) was dispersed in ultrapure water (30 mL) in a quartz reactor (50 mL). Pure $CO_2$ gas was introduced into the mixture for 30 minutes. During the reaction, the temperature of the reaction solution was controlled by an external water stream to maintain a temperature of 25°C. The system was then irradiated under simulated sunlight using a PLS-SXE300 Xe lamp with an AM 1.5 cutoff filter. In addition, the liquid products in the liquid phase of the reactor were measured and analyzed for HCOOH by ion chromatography, and the gaseous products were analyzed by gas chromatography.

**Photocatalytic experiment for CPR.**

TiO2/MXene-MF or TiO2/MXene-CMF was placed in a reaction vessel and 10 mL of reaction volume solution (water, seawater, sewage water) was added, making sure that the solution was about 1 cm away from the 2D catalytic layer, and pure CO2

gas was passed into the mixture for 30 minutes. During the reaction, the temperature of the reaction solution is controlled by an external stream of water to maintain it at about 25°C. The temperature of the reaction solution is then controlled by an external stream of water. The system was then irradiated under simulated sunlight using a PLS-SXE300 xenon lamp with an AM 1.5 cut-off filter. In addition, the liquid product HCOOH and the gaseous product GC in the liquid phase of the reactor were measured and analyzed using ion chromatography.

**Electrochemical tests**

Photocurrent, electrochemical impedance spectroscopy, and Mott Schottky measurements were performed in a three-electrode electrochemical workstation system (CHI 660e) with an ITO glass substrate (1 cm × 1 cm) as the working electrode, a platinum wire as the auxiliary electrode, and an Ag/AgCl electrode as the reference electrode. The sample (5 mg) was dispersed in a solution (1 mL) containing Nafion solution (60 uL, 0.5 wt%) and ethanol (940 uL). After sonication, the dispersed aqueous slurry was drop-cast onto an ITO glass substrate. The working electrode was then dried naturally at room temperature. A 0.2 M $Na_2SO_4$ solution was used as the electrolyte. Photocurrent measurements were performed using a 300 W xenon lamp with a cutoff frequency of AM 1.5.

**Characterization.**

The crystal structure and phase composition of the samples were determined by X-ray powder diffractometer using Cu Ka radiation at 40 KV and 40 mA (Bruker D8 ADVANCE). A transmission electron microscope was operated at 200 kV and TEM

images were obtained (Talos F200X). Diffuse reflectance spectra were recorded by a UV-Vis-NIR spectrophotometer and a resolved infrared spectrometer (PE Lambda 950, Bruker INVENIO X). XPS measurements were performed using an Al Ka monochromatic X-ray radiation source (AXIS ULtrabld).

# References


1 Kamada, K. *et al.* Photocatalytic CO2 Reduction Using a Robust Multifunctional Iridium Complex toward the Selective Formation of Formic Acid. *J Am Chem Soc* **142**, 10261-10266 (2020). https://doi.org:10.1021/jacs.0c03097

2 Xie, B. *et al.* Synergistic ultraviolet and visible light photo-activation enables intensified low-temperature methanol synthesis over copper/zinc oxide/alumina. *Nat.Commun.* **11**, 1615 (2020). https://doi.org:10.1038/s41467-020-15445-z

3 Li, X. *et al.* Accessing parity-forbidden d-d transitions for photocatalytic CO(2) reduction driven by infrared light. *Nat.Commun.* **14**, 4034 (2023). https://doi.org:10.1038/s41467-023-39666-0

4 Ma, W. *et al.* Synergistic Interplay of Dual-Active-Sites on Metallic Ni-MOFs Loaded with Pt for Thermal-Photocatalytic Conversion of Atmospheric CO2 under Infrared Light Irradiation. *Angewandte Chemie International Edition* (2023). https://doi.org:10.1002/anie.202313784

5 Vasilyev, D. V. & Dyson, P. J. The Role of Organic Promoters in the Electroreduction of Carbon Dioxide. *ACS Catalysis* **11**, 1392-1405 (2021). https://doi.org:10.1021/acscatal.0c04283

6 Tang, J. *et al.* Selective hydrogen peroxide conversion tailored by surface, interface, and device engineering. *Joule* **5**, 1432-1461 (2021). https://doi.org:10.1016/j.joule.2021.04.012

7 Dai, C. *et al.* Selective Electroreduction of Carbon Dioxide to Formic Acid on Cobalt-Decorated Copper Thin Films. *Small Methods* **3** (2019). https://doi.org:10.1002/smtd.201900362

8 Dong, L. Z. *et al.* Stable Heterometallic Cluster-Based Organic Framework Catalysts for Artificial Photosynthesis. *Angew Chem Int Ed Engl* **59**, 2659-2663 (2020). https://doi.org:10.1002/anie.201913284

9 Francke, R., Schille, B. & Roemelt, M. Homogeneously Catalyzed Electroreduction of Carbon Dioxide-Methods, Mechanisms, and Catalysts. *Chem Rev* **118**, 4631-4701 (2018). https://doi.org:10.1021/acs.chemrev.7b00459

10 Mo, S. *et al.* Non-interacted Ni and Fe Dual-atom Pair Sites in N-doped Carbon Catalysts for Efficient Concentrating Solar-driven Photothermal CO2 reduction. *Angewandte Chemie International Edition* (2023). https://doi.org:10.1002/anie.202313868

11 Dutt, A. *et al.* Experimental band structure spectroscopy along a synthetic dimension. *Nat.Commun.* **10**, 3122 (2019). https://doi.org:10.1038/s41467-019-11117-9

12 Chen, Y. *et al.* Cooperative catalysis coupling photo-/photothermal effect to drive Sabatier reaction with unprecedented conversion and selectivity. *Joule* **5**, 3235-3251 (2021). https://doi.org:10.1016/j.joule.2021.11.009

13 Kamakura, Y. *et al.* Tin(II)-Based Metal-Organic Frameworks Enabling Efficient, Selective Reduction of CO(2) to Formate under Visible Light. *Angew Chem Int Ed Engl*, e202305923 (2023). https://doi.org:10.1002/anie.202305923

14 Wang, L. *et al.* Black indium oxide a photothermal CO2 hydrogenation catalyst. *Nat.Commun.* **11**, 2432 (2020). https://doi.org:10.1038/s41467-020-16336-z

15 Zhang, H. *et al.* An unprecedent hydride transfer pathway for selective photocatalytic reduction of CO2 to formic acid on TiO2. *Applied Catalysis B: Environmental* **284** (2021). https://doi.org:10.1016/j.apcatb.2020.119692

16 Zhao, Y. *et al.* Solar- versus Thermal-Driven Catalysis for Energy Conversion. *Joule* **3**, 920-937 (2019). https://doi.org:10.1016/j.joule.2019.03.003

17 Lee, W. H. *et al.* Floatable photocatalytic hydrogel nanocomposites for large-scale solar hydrogen production. *Nat Nanotechnol* (2023). https://doi.org:10.1038/s41565-023-01385-4

18 Li, J. *et al.* Non-Lignin Substrate Constructing the Gas-Solid Interface For Enhancing The Photothermal Catalytic Water Vapor Splitting. *Adv.Mater.*, e2305535 (2023). https://doi.org:10.1002/adma.202305535

19 Sun, R. *et al.* Heterogeneous catalysts for CO2 hydrogenation to formic acid/formate: from nanoscale to single atom. *Energy Environ. Sci.* **14**, 1247-1285 (2021). https://doi.org:10.1039/d0ee03575k

20 Zhou, J. *et al.* Linking oxidative and reductive clusters to prepare crystalline porous catalysts for photocatalytic CO2 reduction with H2O. *Nat.Commun.* **13**, 4681 (2022). https://doi.org:10.1038/s41467-022-32449-z

21 Zhou, L. *et al.* Light-driven methane dry reforming with single atomic site antenna-reactor plasmonic photocatalysts. *Nature Energy* **5**, 61-70 (2020). https://doi.org:10.1038/s41560-019-0517-9

22 Li, K. *et al.* Highly efficient photocatalytic H2O2 production in microdroplets: accelerated charge separation and transfer at interfaces. *Energy Environ. Sci.* **16**, 1135-1145 (2023). https://doi.org:10.1039/d2ee03774b

23 Wang, J. *et al.* Customized Microenvironments Spontaneously Facilitate Coupled Engineering of Real-Life Large-Scale Clean Water Capture and Pollution Remediation. *Adv.Mater.*, e2306103 (2023). https://doi.org:10.1002/adma.202306103

24 Kim, C. *et al.* Accelerating the net-zero economy with CO2-hydrogenated formic acid production: Process development and pilot plant demonstration. *Joule* **8**, 693-713 (2024). https://doi.org:10.1016/j.joule.2024.01.003

25 Loh, J. Y. Y., Kherani, N. P. & Ozin, G. A. Persistent CO2 photocatalysis for solar fuels in the dark. *Nature Sustainability* **4**, 466-473 (2021). https://doi.org:10.1038/s41893-021-00681-y

26 Wei, D., Sang, R., Sponholz, P., Junge, H. & Beller, M. Reversible hydrogenation of carbon dioxide to formic acid using a Mn-pincer complex in the presence of lysine. *Nature Energy* **7**, 438-447 (2022). https://doi.org:10.1038/s41560-022-01019-4

27 Qin, X. *et al.* Direct conversion of CO and H2O to hydrocarbons at atmospheric pressure using a TiO2−x/Ni photothermal catalyst. *Nature Energy* (2024). https://doi.org:10.1038/s41560-023-01418-1

28 Ren, Y. *et al.* Concentrated solar CO(2) reduction in H(2)O vapour with >1% energy conversion efficiency. *Nat.Commun.* **15**, 4675 (2024). https://doi.org:10.1038/s41467-024-49003-8

29 Wang, Y. *et al.* Direct and indirect Z-scheme heterostructure-coupled photosystem enabling cooperation of CO2 reduction and H2O oxidation. *Nat.Commun.* **11**, 3043 (2020). https://doi.org:10.1038/s41467-020-16742-3

30 Tsallis, C., Sa Barreto, F. C. & Loh, E. D. Generalization of the Planck radiation law and application to the cosmic microwave background radiation. *Phys Rev E Stat Phys Plasmas Fluids Relat Interdiscip Topics* **52**, 1447-1451 (1995). https://doi.org:10.1103/physreve.52.1447

31 Ghidiu, M., Lukatskaya, M. R., Zhao, M. Q., Gogotsi, Y. & Barsoum, M. W. Conductive two-dimensional titanium carbide 'clay' with high volumetric capacitance. *Nat.* **516**, 78-81 (2014). https://doi.org:10.1038/nature13970

32 Ren, G., Zhou, M., Hu, P., Chen, J. F. & Wang, H. Bubble-water/catalyst triphase interface microenvironment accelerates photocatalytic OER via optimizing semi-hydrophobic OH radical. *Nat.Commun.* **15**, 2346 (2024). https://doi.org:10.1038/s41467-024-46749-z

33 Gallis, M. A., Torczynski, J. R. & Rader, D. J. Molecular gas dynamics observations of Chapman-Enskog behavior and departures there from in nonequilibrium gases. *Phys Rev E Stat Nonlin Soft Matter Phys* **69**, 042201 (2004). https://doi.org:10.1103/PhysRevE.69.042201

## Supplementary Files

This is a list of supplementary files associated with this preprint. Click to download.

- Supportinginformation.docx